



Revealing an unexpectedly low electron injection threshold via reinforced shock acceleration

Received: 20 May 2024

Accepted: 19 December 2024

Published online: 13 January 2025

Check for updates

Savvas Raptis¹✉, Ahmad Lalti^{2,3,4}, Martin Lindberg^{5,6}, Drew L. Turner¹, Damiano Caprioli¹⁷ & James L. Burch¹⁸

Collisionless shock waves, found in supernova remnants, interstellar, stellar, and planetary environments, and laboratories, are one of nature's most powerful particle accelerators. This study combines *in situ* satellite measurements with recent theoretical developments to establish a reinforced shock acceleration model for relativistic electrons. Our model incorporates transient structures, wave-particle interactions, and variable stellar wind conditions, operating collectively in a multiscale set of processes. We show that the electron injection threshold is on the order of suprothermal range, obtainable through multiple different phenomena abundant in various plasma environments. Our analysis demonstrates that a typical shock can consistently accelerate electrons into very high (relativistic) energy ranges, refining our comprehension of shock acceleration while providing insight on the origin of electron cosmic rays.

Understanding how charged particles in the universe gain immense energy, reaching relativistic levels, remains a fundamental challenge in modern physics. Collisionless shocks are ubiquitously found throughout the universe (e.g., heliospheric¹, astrophysical^{2,3}, planetary⁴, and laboratory⁵) and are considered to be the primary drivers of accelerating charged particles to such an energetic regime⁶. Therefore, they have been the main focus of research for understanding the cosmic ray (ultra-relativistic particles) profiles observed on Earth. Shock Drift Acceleration (SDA) occurs when a charged particle encounters a collisionless shock. This mechanism can typically accelerate electrons to relatively high energies, but it is not sufficient to explain the observations of relativistic electrons⁷. Diffusive Shock Acceleration (DSA), known as the first-order Fermi mechanism, can accelerate particles to relativistic energies⁸. However, to get particles efficiently accelerated through DSA, they need to be pre-energized to a certain threshold before they can be injected into the acceleration process. Ion injection to DSA is sufficiently understood since ions have a large dynamical scale length, comparable to typical shock scales. On

the other hand, electrons due to their much smaller gyroradius, have a higher injection threshold, requiring them to reach mildly relativistic energies (10–100 keV) before they can get further accelerated through DSA. Finding which process consistently allows these energies to be obtained in a collisionless shock is called the electron injection problem and remains one of the open questions of modern physics^{9–11}.

The dynamics of a collisionless shock depend greatly on a key property, the angle between the shock normal vector and the magnetic field in the upstream plasma (θ_{Bn})¹². In a typical plasma consisting of electrons and protons, when this angle is approximately less than 45 degrees, protons (and heavy ions) can get reflected, travel far upstream, interact with the incident plasma, and cause a series of instabilities and wave activity forming an extensive region called the foreshock or precursor. The foreshock region consists of a strongly variable and dynamically evolving plasma, while characterized by temporally varying (transient) and spatially localized structures. Subsequently, this extends the shock's presence and intensifies its impact on the nearby plasma. As a result, in our Solar System, quasi-parallel

¹Johns Hopkins University Applied Physics Laboratory, Laurel, MD, USA. ²Northumbria University, Newcastle upon Tyne, UK. ³Swedish Institute of Space Physics, Uppsala, Sweden. ⁴Uppsala University, Uppsala, Sweden. ⁵Division of Space and Plasma Physics - KTH Royal Institute of Technology, Stockholm, Sweden. ⁶Department of Physics and Astronomy, Queen Mary University of London, London, UK. ⁷Department of Astronomy & Astrophysics and E. Fermi Institute, The University of Chicago, Chicago, IL, USA. ⁸Southwest Research Institute, San Antonio, TX, USA. ✉e-mail: savvas.raptis@jhuapl.edu

shocks ($\theta_{Bn} \leq 45^\circ$) typically emerge as notably more efficient particle accelerators compared to quasi-perpendicular ($\theta_{Bn} \geq 45^\circ$) shocks^{4,13,14}. Foreshock transients (or dayside/shock-generated transients) occur multiple times per day¹⁵ and form when the solar wind and its embedded, variable, and discontinuous magnetic field interact with a shock wave, like Earth's bow shock^{15,16}. Foreshock transients are also recognized for their ability to accelerate particles to high energies^{13,14,17}. The transients examined in this study are commonly referred to as Hot Flow Anomalies (HFAs) in heliophysics literature. However, due to their similarities with other transients, such as Foreshock Bubbles (FBs), which also play a role in particle acceleration, we use the more general term 'foreshock transient' throughout the text.

In this work, we propose a potential resolution to the injection problem by showing in situ observations of a comprehensive multistep process operating across various scales, allowing electrons to consistently reach relativistic energies. As we present below, our model refines the traditional shock acceleration processes by introducing findings revealing an electron injection threshold. This result is obtained through encompassing recent advancements in astrophysical plasmas and wave-particle interactions and is generalized to other stellar and interstellar environments.

Results

The model presented in this work relies primarily on in situ observations from two NASA missions. The Magnetospheric Multiscale (MMS) mission¹⁸ provides near-Earth observations, while the Acceleration, Reconnection, Turbulence, and Electrodynamics of Moon's Interaction (ARTEMIS) mission¹⁹ describes the far upstream plasma environment close to the dayside Moon. On December 17, 2017, between 17:50 UT and 17:55 UT, the MMS spacecraft was positioned just upstream of Earth's bow shock and observed an energetic event. MMS recorded a foreshock transient associated with the highest energetic electrons ever observed upstream of the bow shock since its prime mission started in 2015, under relatively steady solar wind conditions. Electrons reached observable intensity enhancements to more than 500 keV, a remarkable feat considering the typical observable range is up to only a few keV in the solar wind near Earth. This observation is unique, as there was an absence of significant solar disturbances, like a flare or a coronal mass ejection (CME), which could otherwise explain the presence of such relativistic electrons. Our findings indicate that the electron acceleration during this event manifested within a foreshock transient. This phenomenon emerged due to a disturbance (discontinuity) in the interplanetary magnetic field, interacting with Earth's bow shock and foreshock plasma. ARTEMIS, positioned in lunar orbit over one hundred thousand kilometers towards the Sun from MMS, observed this magnetic disturbance along with an associated electron seed population a few minutes before the foreshock transient formation.

In Fig. 1, we present an overview plot highlighting the observations, emphasizing the presence of high-energy electrons above the rest mass energy (> 511 keV), as shown in panels (d) and (g). As displayed in panels (a-h) around the green shaded area, a compressive edge is formed resulting in a fast collisionless quasi-perpendicular shock, which is a typical feature of foreshock transients^{14,20}. Another vital feature of the foreshock transient is shown around the purple shaded area, where the core of the structure is infused by high-amplitude electromagnetic waves over a wide range of frequencies (illustrated in Fig. 2), in a low-density plasma environment. This wave and topological environment facilitates electron scattering, enabling them to cross the shock (green shaded area) multiple times, where typical shock acceleration mechanisms occur (i.e., DSA/SDA)^{9,21}. However, in contrast to theoretical and observational expectations of quasi-perpendicular SDA²¹, in panel (h), the energy power law spectral index reaches canonical values up to $p = -2$, which is the theoretical prediction for DSA at strong shocks²²⁻²⁴. This indicates that the

acceleration observed upstream of the planetary bow shock results in an even harder spectrum than what would typically be produced by a classical DSA mechanism. One direct explanation for this observation is that in foreshock transients, the wave field is found in a lower background magnetic field than in a typical downstream shocked plasma, allowing particles to become more efficiently scattered and subsequent acceleration to take place^{25,26}. Moreover, these electrons can exhibit a bouncing behavior between Earth's nearby shock environment and the foreshock transient. This interplay results in ideal confinement, enhancing the effectiveness of acceleration compared to a typical quasi-perpendicular shock^{13,25,26} while other factors, such as the presence of electrostatic waves can also play a role in the scattering of particles near the shock transition²⁷⁻²⁹.

In Fig. 2, a crucial factor reinforcing the shock acceleration process is unveiled. Specifically, by analyzing the compressive (shock) region of the foreshock transient, the interaction between high-frequency, high-amplitude, banded emissions of nonlinear electromagnetic waves and the local electron populations is shown. Panel (c) of Fig. 2 displays a notable electron temperature anisotropy ($A = 1 - T_{per}/T_{par} < 0$) known to drive large-amplitude, high-frequency electromagnetic waves, termed whistlers (or chorus in magnetospheric research nomenclature), which can experience instability and wave growth from electron betatron acceleration localized within the compression region^{14,30}. The presence and characteristics of these waves enable higher energy electrons to cyclotron resonate with them, amplifying the electrons' energy through wave-particle interactions³¹, thereby further enhancing the shock acceleration process³². This phenomenon has been observed in magnetospheric environments^{32,33} and recently in collisionless shocks³⁰. The nature of these waves is identified by the characteristic narrowband frequency in the magnetic field power spectra between 0.1 and 1.0 of the local electron cyclotron frequency (panels e and f), the right-hand polarization (panel g), and the propagation parallel to the magnetic field (panel h). Finally, cyclotron-resonant acceleration of relativistic electrons is expected to result in a predominantly perpendicular (with respect to the background magnetic field) acceleration^{32,33}. As shown in panel (h), the pitch angle distribution (PAD) confirms this theoretical expectation. The electron's pitch angle distribution peaks at 90 degrees with respect to the local magnetic field as soon as the spacecraft crosses the wave acceleration region, in agreement with the wave-particle acceleration model. It should be noted that other mechanisms, such as betatron acceleration, could produce similar pitch angle distributions (PADs) and are expected to contribute to the observed acceleration. However, evaluating the contribution of each mechanism is not feasible observationally and falls outside the scope of this study.

At this point, we have confirmed the presence of multiple acceleration and confinement components taking place from small (i.e., plasma kinetic) to large (global with respect to Earth's bow shock within the solar wind) scales. Specifically, we have shown the presence of shock acceleration in the foreshock transient^{13,14}, a strong wavefield and confining region^{25,26}, and nonlinear wave-particle interactions and acceleration between the electromagnetic whistler waves and the electron distribution^{30,34}. Furthermore, the environment between the primary planetary bow shock and the foreshock transient creates a larger bounded environment in which the particles can remain confined, bouncing between the regions^{13,25}, this is particularly true for magnetic field discontinuities that intersect the bow shock under certain geometries like in our case (see "Methods", subsection Statistical analysis details), these elements cannot entirely explain the distinctive presence of electrons with energies of 500 keV, nor the occasional absence of such particle population during foreshock transients with similar characteristics²⁵. Hence, we further explored the possibility of identifying whether a specific seed population, well beyond the vicinity of Earth's bow shock environment, was present, corresponding to global system size effects. From a multi-case study

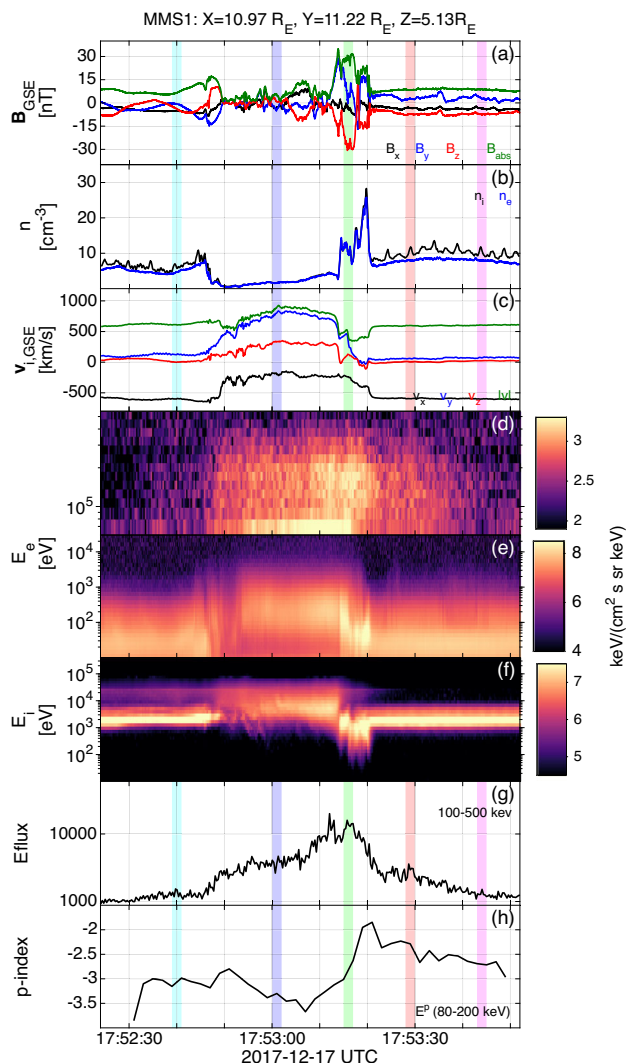
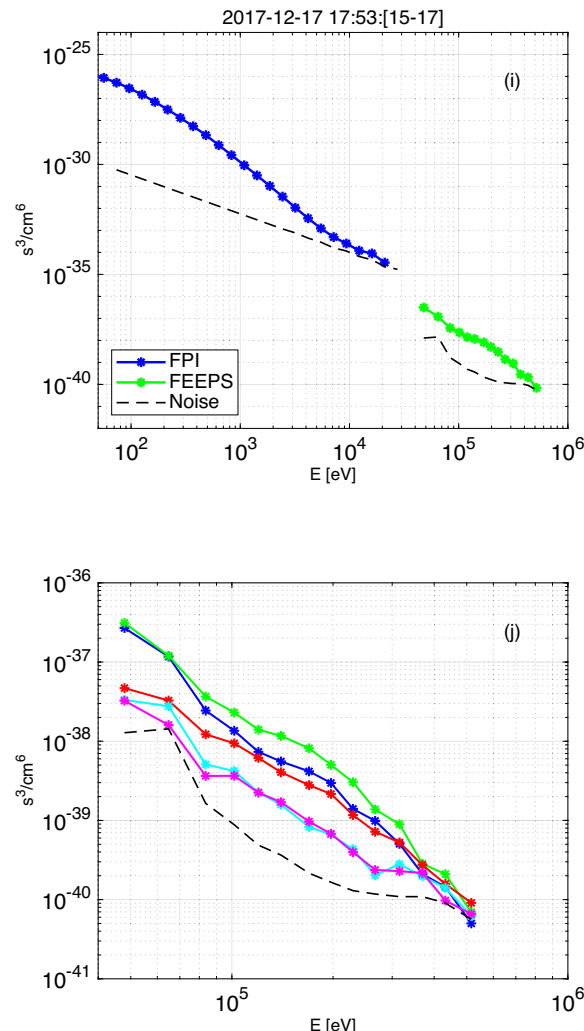


Fig. 1 | Overview observations of the main electron acceleration event.

a magnetic field components and magnitude in a Geocentric Solar Ecliptic (GSE) system, (b) ion and electron densities, (c) ion plasma velocity components and magnitude in GSE coordinates, (d) high-energy differential energy flux electron spectra, (e) low-mid energy differential energy flux electron spectra, (f) combined differential energy flux ion spectra, (g) integrated energy electron flux between 100 and 500 keV, (h) fitted spectra index for E^p between 80–200 keV, (i) electron phase space density (PSD) versus energy for the whole energy range along with background noise level, (j) series of PSD versus energy line plots for high-energy measurements over different time intervals along with the background noise level limit.

described below, our investigation revealed a clear increase in the suprathermal electron flux (1–5 keV) measured by the ARTEMIS spacecraft in dayside lunar orbit, during all the foreshock transient events associated with electron acceleration, as observed by MMS. In addition, this seed electron population was associated with the faster-than-average solar wind, typical of what emerges from solar coronal holes at higher solar latitudes, resulting in high-speed plasma streams^{35–37}.

To validate our model, we extensively reviewed all available observations from the operational years of MMS. While observational limitations were present (MMS required to be upstream of the shock with burst data availability and ARTEMIS in dayside far-upstream lunar orbit), we found several events aligning, either partially or fully, with our model components. Upon analysis, we noticed a distinct pattern. Whenever MMS recorded electron fluxes exceeding 100 keV upstream of the bow shock, ARTEMIS detected a clear seed population of



The colors of the panel (j) are indicated as highlighted areas in the time series plot of panels (a–h). The event is observed from 17:52:45 to 17:53:25. Panels (d) and (g) show a distinct enhancement of relativistic energies in the 100–500 keV range. The green shaded area around 17:53:15–20 shows the area that has the strongest acceleration. The electron enhancement there can be seen compared to other times by looking at panel (j). The title shows the location of the MMS spacecraft in GSE coordinates given in Earth radius units. More information regarding the derivation of each product can be found in methods, subsection Data post-process and derivations.

suprathermal, solar wind electrons. This trend consistently occurred when the solar wind originated from the Sun's coronal holes, typically referred to as fast solar wind^{35–38}. Our findings were further supported by the increased occurrence of magnetic field discontinuities and overall variability (necessary ingredients for the formation of foreshock transients) in fast solar wind plasma^{39,40}. In all events associated with fast coronal hole plasma, the suprathermal electron flux (1–5 keV) was notably elevated, ranging from 2 to 5 times higher than the background level (see Fig. 3). In contrast, slow solar wind events in which no relativistic electron acceleration occurred were lacking an enhanced seed population. As a result, despite the presence of magnetic discontinuities and consequently the formation of foreshock transients, MMS measured primarily background noise on the high-energy particle instruments. The source of the initial seed population could potentially arise from magnetic reconnection in the solar wind⁴¹, turbulence⁴², discontinuities impacting the solar wind plasma⁴³, or

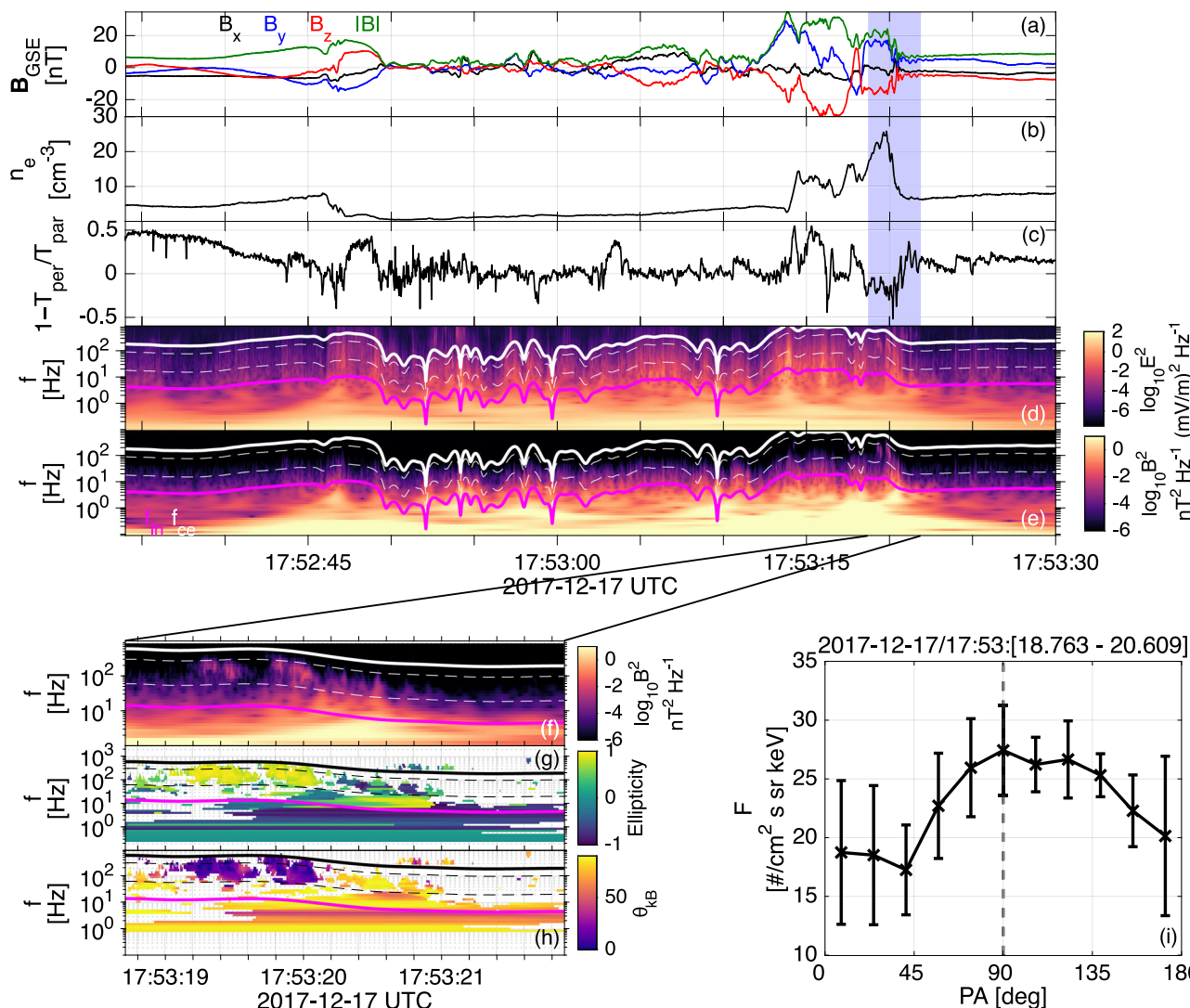


Fig. 2 | Detailed plot of the main electron acceleration event and wave analysis. (a) magnetic field components and magnitude in GSE coordinates, (b) electron density, (c) electron temperature anisotropy, (d) electric field power spectra, (e) magnetic field power spectra, (f) zoomed-in plot of magnetic field power spectra, (g) ellipticity showing the polarization of the magnetic field power spectra, (h) wave propagation angle, (i) pitch angle distribution (PAD) for electrons between 40 and 200 keV averaged over 6 measurements when the wave activity is the strongest as indicated by the date at the title. Error bars represent the Standard Deviation (SD) for each measurement. Nonlinear electron whistler waves are present in the large-amplitude, banded emissions between 0.1 and 1.0 of the electron cyclotron

frequency, f_{ce} , with ellipticity near 1 (red in panel g) and propagation angles parallel to the background magnetic field (blue in panel h). 0.1 and 1.0 f_{ce} are shown with the bottom-most dotted and solid white lines in the wave panels; the magenta line and the middle dashed line in the wave panels are the plasma lower hybrid frequency and 0.5 f_{ce} , respectively. Such nonlinear whistler-mode wave packets are capable of resonantly interacting with relativistic electrons, resulting in predominantly perpendicular acceleration (as shown in panel i). More information regarding the derivation of each product can be found in the methods, subsection Data post-process and derivations.

direct jet outflow from the coronal hole environment⁴⁴. Furthermore, by using the high-energy instrument on board ARTEMIS and removing events flagged by low quality, we confirm that relativistic electrons were not present in lunar orbit for the main event analyzed and for most of the seeded events. This allowed us to rule out the possibilities of pre-accelerated relativistic electrons coming from external origin. Finally, the enhanced suprathermal electron flux at ARTEMIS contains both earthward and sunward components, while the magnetic connectivity to the bow shock takes place only for a couple of cases. This indicates that a significant portion of the observed seed population appears to be of Solar origin. However, the connectivity to the shock and the presence of sunward particles in some cases hints toward an interplay between the solar wind and the Earth's bow shock under which particles from the electron foreshock may contribute to the seeding of the acceleration mechanism (see e.g., ref. 25). More details

are shown in methods, subsection Statistical analysis details. Finally, we should note that while the presence of fast coronal hole (CH) solar wind and associated suprathermal energy elevation is a necessary condition for the acceleration of high-energy electrons, it is not sufficient on its own. There are instances where, despite the fast solar wind conditions, the acceleration mechanisms are limited, resulting in an absence of high-energy (100 + keV) electrons.

To complete our analysis, we investigated whether the energies observed at the most energetic of our events (Figs. 1 and 2) are bounded by diffusion scale lengths of Earth's bow shock environment. For plasma environments with wavefields corresponding to high nonlinearity (i.e., $8B - B_0$) like the foreshock transient's core region (purple shaded area Fig. 1), the diffusion length is approximated by assuming Bohm diffusion⁶. This means that the effective mean free path of electrons in these environments is approximately equal to the

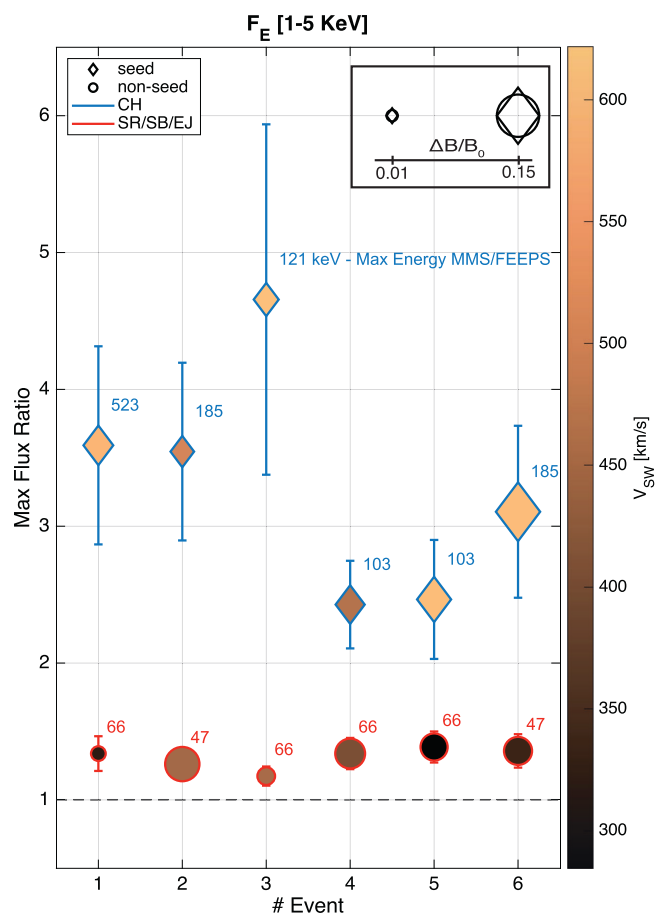


Fig. 3 | Statistical analysis and validation of the reinforced shock acceleration for relativistic electrons. The analysis includes six events with and without the presence of different components that embody our model. The y-axis shows the maximum ratio between the 1–5 keV flux of the seed population with respect to the background from the initial solar/stellar wind, while the x-axis indicates the number of each event. The colorbar shows the bulk flow velocity of the stellar wind, revealing the connection between the high-speed stream and the higher maximum electron flux ratio. The marker color shows if the particles originate from fast stellar wind (blue) or slow stellar wind (red). CH refers to coronal hole plasma, SR to sector reversal, SB to streamer belts, and EJ to ejecta^{36–38}. The marker shape shows the presence of the initial seed enhancement, with a diamond indicating the seeded events and a circle for the non-seeded ones. The different marker size indicates the amplitude of the nonlinear electromagnetic waves compared to the background ($\Delta B/B_0$), while each event is accompanied by text referring to the energy channel for which a significant electron flux was measured above the noise instrument level close to Earth. More information regarding the derivation of each product and the classification of the solar wind can be found in methods, subsection Solar wind origin determination. The exact times for which we took measurements for MMS and ARTEMIS are given in methods, subsection Statistical analysis details. Error bars represent the Standard Deviation (SD), calculated using the intervals described in methods, subsection Data post-process and derivations.

electron gyroradius (i.e., $\lambda \sim r_{ce}$)⁶. Using that, we recovered that for the maximum energy observed (about 0.5 MeV) we obtain, a diffusion length to be in the order of $10\text{--}100 R_e = 6 \cdot 10^{4\text{--}5} \text{ km}$ (see more details in methods, subsection Diffusion time scales and spatial scale sizes) which is on the same order as foreshock transients' scale sizes observed at Earth⁴⁵.

This finding is particularly interesting, as other planetary environments with larger system scale sizes (e.g., Jupiter) can sustain higher obtainable maximum energy. By using a fixed diffusion length and magnetic field, we can calculate the highest energy that an electron can obtain before the scale of its gyroradius is too large for it to remain in

the shock acceleration region. Specifically, by using an approximate diffusion length of $L = 100\text{--}1000 R_e \approx 6 \cdot 10^{5\text{--}6} \text{ km}$ and a background magnetic field of 1 nT, we can obtain higher relativistic energies up to 2 MeV, which is in agreement with previous observations and analysis^{45,46}. It should be noted that this upper energy can be higher in other astrophysical systems (e.g., ultrahot Jupiters⁴⁷). Following the same argumentation as above, our mechanism shows that such a system can sustain electrons in the order of GeV to low TeV range (even when considering synchrotron losses), corresponding to the highest, ultra-relativistic energies of cosmic ray electrons observed at Earth^{48,49}.

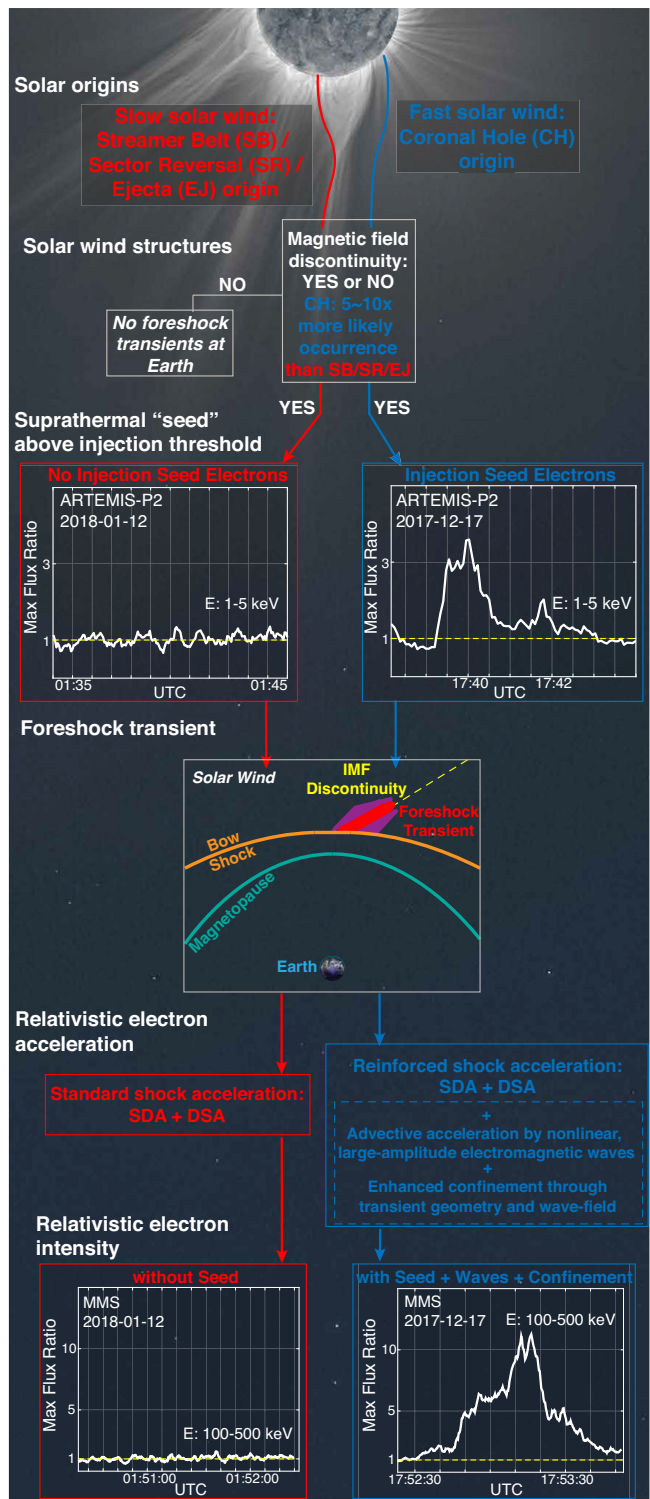
Finally, in Fig. 4, we provide an illustrative summary of the proposed, reinforced shock acceleration model, depicting the evolutionary pathway of two distinct events. The first event, showcased in blue on the right-hand side of the schematic, corresponds to the main seeded event detailed in Figs. 1 and 2 (also referenced as #1 seeded event in Fig. 3). In contrast, the left-hand side of the schematic portrays a non-seeded event (highlighted in red), identified as #1 non-seeded in Fig. 3. This schematic comparison offers a clear visualization of the differences between each possible scenario highlighted by in situ measurements of both ARTEMIS and MMS mission.

Discussion

Our work engendered a unified shock acceleration mechanism applicable to stellar and interstellar plasma environments. First, we revealed a surprisingly low electron injection threshold, observed using in situ space plasma observations. This threshold at Earth's system is found to be in the order of suprathermal range (1–5 keV). These suprathermal electrons occur under fast solar wind conditions and are sufficient to enable a reinforced shock acceleration mechanism. The presence of this seed population allows the foreshock transient to consistently produce relativistic electrons⁵⁰. This is the result of a particularly efficient multiscale process (acceleration efficiency: $\nu = \frac{U_e}{U_i} \approx 0.05 = 5\%$ (see more details on methods, subsection Data post-process and derivations)). On ion kinetic scales, the foreshock transient, along with its compressive edge forms, allows shock acceleration to occur ahead of the primary planetary bow shock^{14,17}. On electron kinetic scales, within the foreshock's shock, wave-particle energy transfer from the nonlinear high-frequency, high-amplitude electromagnetic waves contribute to the acceleration of suprathermal electrons to relativistic energies^{30,34,51}. This resonance mechanism occurs alongside larger-scale processes such as betatron and Fermi acceleration, which take place within the foreshock transient scales^{14,16,25}. Moving to even larger scales, as electrons emerge from the foreshock transient's shock acceleration region, they are confined by the presence of a highly nonlinear wavefield within the foreshock transient's core and by the presence of the primary planetary bow shock that geometrically bound the electrons. We should note that since this whole process is taking place upstream of the primary shock, the already accelerated electrons can get additional energy via shock processes at the primary shock^{9,21,52}.

Undoubtedly, the most important result we showed is that for Earth's shock system, the electron injection threshold in our model can be in the order of low 1–10 keV range (seed population in solar/stellar wind). This relatively low level of energy requirement in electron flux can be achieved through multiple mechanisms, yet it appears to be occurring exclusively under coronal hole solar wind plasma, corresponding to relatively faster than typical solar wind conditions. As the solar activity is approaching its maximum (2024–2025), we expect solar-focused missions such as Parker Solar Probe (PSP) and Solar Orbiter in conjunction with magnetospheric missions to shed light on the nature and origin of this seed population embedded within the high-speed solar wind stream.

In addition, our results enhance the understanding of electron acceleration by providing a clear explanation for past observations of



relativistic electrons on Earth. Previously, these cases were puzzling due to their unusually high-energy populations. By re-evaluating the three events discussed in ref. 17 and the event in ref. 14, we identify consistent conditions across all four events. Specifically, each event observed by THEMIS, like our findings, is associated with a distinct fast coronal hole solar wind. In the few cases where ARTEMIS provided undisturbed upstream data, an elevated suprathermal electron flux was also observed. This insight is crucial, as it clarifies the unique nature of these foreshock transients, supporting our conclusions, and providing the missing piece needed to explain previous results.

Fig. 4 | Schematic of the reinforced shock acceleration mechanism. The process unfolds in several steps, illuminating the distinctions between two distinct events: the primary seeded event marked in blue and a non-seeded event in red. The first step is the fueling of the process, originating directly from the Sun's activity, in which the fast solar wind plasma provides a seed population above the electron injection threshold (1–5 keV) associated with magnetic field discontinuities as measured by the ARTEMIS mission during its dayside Lunar orbit. The next step involves a Fermi-type shock (i.e., DSA) and/or shock drift (SDA) acceleration, occurring at the sunward-facing shock within a foreshock transient. This transient arises after the discontinuity interacts with Earth's bow shock. The acceleration of electrons is further enhanced by the presence of wave-particle interactions between electrons and high-amplitude, high-frequency electromagnetic waves. Lastly, the process's efficiency is intensified by particle scattering and confinement within the local magnetic topology of the transient and its connectivity to the primary shock (i.e., Earth's bow shock in this case). Electromagnetic waves within the foreshock effectively scatter particles back to the acceleration region, while the surrounding shock's geometry acts as a confining boundary, enabling electrons to accumulate and obtain relativistic energies before reaching Earth and being lost to the downstream medium. The image of the Sun was taken during a solar eclipse, and credits are attributed to Miloslav Druckmüller, Peter Aniol, and Shadia Habbal <http://www.zam.fme.vutbr.cz/druck/ecl2009e/0-info.htm>.

Moving on, the generalization of this model is straightforward, since its ingredients are essentially fundamental astrophysical plasma processes (collisionless shocks and wave-particle interactions). The presence of the foreshock transients within our Solar System is also consistently found in all planetary systems where sufficient in situ measurements are available. Furthermore, the transients' size scales with the planetary system size, allowing more efficient acceleration to occur in larger collisionless shock systems^{45,46,53,54}. Within our Solar System, the larger system size of gas giants (e.g., Jupiter) allows our mechanism to sustain the energization of particles up to the MeV range, consistent with previous observations. However, further evaluation by the planetary research community is crucial for the validation of our work and for the unification of Heliophysics subdomains.

Apart from addressing electron acceleration within our Solar System, the implications of this model are directly influencing the origin of the electron cosmic ray profile. Cosmic rays are thought to originate from high-mach number supernova shocks ($M_A > 10$)⁵⁵, although determining the exact details is an active research topic. However, it should be noted that even higher Mach number shock waves can be found in other planetary systems (e.g., Saturn⁴ and Jupiter⁵⁶), while collisionless bow shock environments with similar intrinsic properties are found in the interstellar medium around young stellar systems⁵⁷. More importantly, in other stellar systems, under the presence of exoplanets like ultrahot Jupiters⁴⁷, the existence of massive magnetic fields enables our mechanism to potentially sustain GeV-TeV electrons. It should be noted that for young stellar systems, the stellar wind can carry even stronger magnetic fields, that could sustain electrons to even higher energy ranges. Our results, therefore, imply that a portion of the cosmic ray distribution of relativistic electrons might originate from the interaction of planetary quasi-parallel shocks with typical stellar winds. This energy range is well within what is considered to be the ultra-relativistic electron range of cosmic rays. Further investigation should be made by the stellar astrophysics and particle acceleration communities to determine whether such unique systems (young stellar environments with ultra-hot Jupiters) can have a larger contribution to the ultra-relativistic electron spectra through the utilization of the reinforced shock acceleration model. These stellar environments would, therefore, be particularly good candidates to investigate by looking for potential synchrotron emission. This implication originates directly from our model, and its validity needs to be studied in the future, especially since, up to today the main sources of these relativistic energies have been either pulsars or

supernovas^{58,59}. To fully address this impact, future endeavors will require coordinated cross-disciplinary efforts by the Heliophysics and Astrophysical communities, through the use of both remote sensing observations and computer simulations. Future research in Earth's geospace environment could benefit from incorporating solar wind monitors at the Lagrangian 1 (L1) point alongside near-Earth observations from MMS and THEMIS. This approach would provide a more direct connection between coronal hole solar wind and the seed population. In addition, large-scale global simulations that include nonlinear kinetic processes are needed to quantify the precise effects and relative contributions of each acceleration mechanism and scattering/confining process demonstrated in our observations.

Finally, by reinforcing the acceleration processes at quasi-parallel shocks and by evaluating the electron injection threshold for obtaining relativistic electrons at Earth at suprathermal energy ranges, our model ultimately supports the role of quasi-parallel shocks as the source of the ultra-relativistic cosmic ray profile⁶⁰.

Methods

Data

For Magnetospheric Multiscale (MMS) data¹⁸, we used burst resolution Level-2 data from the Fast Plasma Investigation (FPI), Flux Gate Magnetometer (FGM), Search Coil Magnetometer (SCM), Fly's Eye Energetic Particle Spectrometer (FEEPS). For the position of the spacecraft, we used the Magnetic Ephemeris Coordinates (MEC). For Acceleration, Reconnection, Turbulence, and Electrodynamics of Moon's Interaction (ARTEMIS) measurements¹⁹, we used the Flux Gate Magnetometer (FGM), Solid State Telescope (SST), and the Electrostatic Analyzer (ESA) and the state data for its position. Due to the close configuration of the MMS1-4 and ARTEMIS P1-P2, we primarily used MMS1 and ARTEMIS P2 for the analysis shown in the manuscript unless stated otherwise. In addition, for validation purposes, we used OMNIweb data to characterize the global scale of the solar wind conditions. The products used are the 1-h dataset and then propagated to the bow shock 1 min one, both accessible via <https://spdf.gsfc.nasa.gov/pub/data/omni/>. To download the level 2 dataset used in this study, we used the software described in the code availability section.

Coordinates system and spacecraft position

Determining the connection between the MMS and ARTEMIS data required the use of position data for each spacecraft. We used the position of each satellite in Geocentric Solar Ecliptic (GSE) coordinates. In this system, the X-axis is on the Sun-Earth line, while the Y-axis lies on the ecliptic plane towards dusk. The Z-axis completes the coordinate system by being perpendicular to the ecliptic plane. The position of the spacecraft during the main event in GSE coordinate and in Earth Radius units ($R_E \approx 6371$ km) is given as: MMS1: [10.8, 11.1, 5.1] and ARTEMIS P2: [65.2, -5.3, 5.1]. Upon using the solar wind velocity (V_{SW}) and convection along the X-GSE axis, we obtained an estimate of the time lag between the two spacecraft of about 10–15 mins (by simply equating $V_{SW} = \frac{\Delta x}{\Delta t}$, where Δx denotes the distance of the two spacecraft along the X-GSE axis, and Δt the time lag between their measurements). The rest of the MMS satellites (i.e., MMS2-4) are located in a close tetrahedron formation within a few kilometers of each other. This close formation allows multi-spacecraft methods such as timing to be used throughout our analysis, which is a typical method used in multi-spacecraft research^{20,21}. It should be noted that the positions of ARTEMIS and MMS are very different for each event (see "Methods" subsection Statistical analysis details). This results in a time lag between the spacecraft that can vary from instantaneous observations to tens of minutes, depending on the orientation of the magnetic field discontinuity with respect to the plane MMS and ARTEMIS reside. Essentially, the 3D geometry of the magnetic field and the fact that discontinuities are planar structures allow any kind of time lag between the signals (see more details in the following subsections).

Table 1 | The different energy channels measuring electron energies for MMS1, MMS2, and MMS3

Channel	MMS1 (keV)	MMS2 (keV)	MMS3 (keV)	MMS1-3 (keV)	Combined Channels
1	61.2	31.2	27.2	-	(-, -, -)
2	79.9	49.9	45.9	47.9	(-, 2, 2)
3	98.6	68.6	64.6	64.8	(1, 3, 3)
4	117.4	87.4	83.4	83.6	(2, 4, 4)
5	135.1	105.1	101.1	101.6	(3, 5, 5)
6	153.2	123.2	119.2	119.9	(4, 6, 6)
7	174.5	144.5	140.5	140	(5, 7, 7)
8	199.3	169.3	165.3	169.7	(7, 8, 8)
9	228.2	198.2	194.2	197.2	(8, 9, 9)
10	262	232	228	229.4	(9, 10, 10)
11	301.4	271.4	267.4	266.9	(10, 11, 11)
12	347.4	317.4	313.4	315.4	(-, 12, 12)
13	401.2	371.2	367.2	369.2	(-, 13, 13)
14	464	434	430	432	(-, 14, 14)
15	537.2	507.2	503.2	515.9	(15, 15, 15)

The dash (-) sign indicate that no channel (or value) was used.

The two rightmost columns show the combined energy channels (MMS1-3) and which individual MMS channels have been combined to form a common energy bin.

Data post-process and derivations

Before using the high-energy electron differential energy flux data, obtained from the FEEPS instrument, the data need to be cleaned from contamination. This is done by inspecting the MMS1-4 measurements. The MMS4 data typically, and also in our case, have measurable contamination, which made us choose to discard them in our study (see Supplementary Fig. 1). The contamination can be clearly seen in the last panel of the left column. Looking at the MMS2 data (second panel left), one can see the unphysical high flux values appearing every 20 s due to the spin of the spacecraft. The final (cleaned) MMS1-3 data are then shown in the three right panels of Supplementary Fig. 1.

The energy bins of FEEPS for each of the MMS spacecraft are slightly different for the electron differential energy flux. Therefore, when combining the cleaned FEEPS electron data of MMS1-3, the energy channels need to be combined properly. Table 1 shows the individual spacecraft energy bins and the resulting combined ones.

The noise level of the FEEPS high energy electron spectra (shown in Fig. 1i, j) is obtained by a 15 s average window between 17:58:[10–25] on the 2017-12-17 UTC. This set of data is observed to have little to no counts and is located not too far away in time from our event, and is therefore ideal to use as a measure of the instrument(s) noise level. The noise level of the FPI electron flux (Fig. 1i) is determined in the same way but for the FPI instrument. However, due to the consistently high count rate observed at energies below 10 keV, the procedure is only done for energy channels above 10 keV. For energy channels less than 10 keV, the noise level is extrapolated linearly using a linear fit obtained from the observed noise data above 10 keV. Fig. 1 shows the combined ion spectra of the FPI (6 eV–30 keV) and FEEPS (60–600 keV) instruments. The gap of no data between 30–60 keV is exponentially interpolated by assuming an exponential decay between the highest FPI channel and the lowest FEEPS channel.

The spectral index calculated in Fig. 1h is calculated by a fitting process on the phase space density (PSD) profiles for energies between 80–200 keV. The PSD profiles are obtained from 2 s averages evenly spaced between 17:52:30 and 17:52:50 using the electron differential energy flux data shown in Fig. 1. The electron energy flux is converted

Table 2 | The first four columns show probabilities for each classification made for the presented events (Fig. 3) through a Gaussian process (GP) supervised machine learning model³⁸

	Ejecta (EJ)	Coronal Hole (CH)	Sector Reversal (SR)	Sector Reversal (SR)	$\delta B/B_0$
#1 seed	0.07	0.78	0.09	0.06	0.0596
#2 seed	0.10	0.40	0.15	0.23	0.0375
#3 seed	0.07	0.79	0.09	0.05	0.0420
#4 seed	0.13	0.39	0.12	0.37	0.0570
#5 seed	0.07	0.77	0.10	0.07	0.0779
#6 seed	0.06	0.79	0.09	0.06	0.1314
#1 no-seed	0.02	0.09	0.09	0.80	0.0145
#2 no-seed	0.35	0.18	0.05	0.42	0.0789
#3 no-seed	0.56	0.06	0.14	0.23	0.0209
#4 no-seed	0.13	0.12	0.31	0.44	0.0597
#5 no-seed	0.20	0.01	0.63	0.16	0.0493
#6 no-seed	0.25	0.05	0.24	0.46	0.0528

The bold text indicates the most probable (i.e., dominant) class.

Each cell indicates the probability in decimal number format. For this table, we used the OMNI 1 h dataset. The last column indicates wave amplitude with respect to the background magnetic field for each of the events shown in Fig. 3.

into PSD using the following formula⁴¹:

$$f = 1.6 \cdot 10^{-40} \cdot \frac{J}{E^2(E+1.02)} [s^3/cm^6] \quad (1)$$

where E is the particle energy given in MeV and J in cm⁻²s⁻¹sr⁻¹.

To determine the electron acceleration efficiency, we need to estimate the total energy carried by solar wind and then which portion is transferred to the suprathermal electrons. The suprathermal electron energy density can be calculated using the expression:

$$U_e = 4\pi \sqrt{2/m_e} \int_{E_0}^{E_{max}} f_e(E) \sqrt{E^3} dE \quad (2)$$

Where we set the initial suprathermal energy to be $E_0 = 100$ eV and the maximum (E_{max}) to be the maximum energy the FEEPS instrument can measure (515 keV). $f_e(E)$ denotes the phase space density of electrons at that energy, and m_e is the electron mass.

For the solar wind, it is easy to calculate the energy density upstream of the compressive edge of the foreshock transient structure through the expression $U_i = n_i m_i V_{SW}^2 / 2$, where n_i is the ion number density, V_{SW} is the ion speed in the spacecraft reference frame, and m_i is taken to be equal to the proton mass as it is the dominating population in the solar wind.

To compute these two expressions, we need to take the electron distribution when the spacecraft probes the acceleration region to estimate the suprathermal electron part, and in the upstream region for the solar wind. These regions are shown in detail in Fig. 1. Specifically, they correspond to 2017-12-17 17:53:[15-17] UTC for U_e and 2017-12-17 17:53:[30-50] UTC for U_i . For the solar wind upstream region, we took the number density to be $n_i = 10$ [cm⁻³] and $V_{SW} = 600$ km/s which are also typical values of the fast solar wind. By using these values, we obtain the electron acceleration efficiency to be:

$$\nu = \frac{U_e}{U_i} \sim 0.05 = 5\% \quad (3)$$

It should be noted that this definition aligns with what is commonly referred to as acceleration efficiency in the literature. This means that it describes the portion of particles that are above the suprathermal range (i.e., 100 eV in our case). If however, we take E_0 to

be higher so that it corresponds to relativistic regimes (e.g., 1 keV), the efficiency drops to less than 0.5%.

Solar wind origin determination

To determine the origin of the solar wind, we used the classification scheme described in ref. 36. In this work, the solar wind is classified into four categories. Ejecta (EJ), Coronal hole (CH), Sector reversal (SR), and Streamer belts (SB). With CH essentially consisting of fast solar wind plasma, SR and SB indicate slow solar wind conditions, and ejecta are transient phenomena such as Coronal Mass Ejections (CMEs).

At first, we evaluated the statistical properties of solar wind conditions as measured by both OMNIweb data in 1 h and 1 min resolution. In addition, to make sure that the classification is accurate and does not depend on instrumentation variation, we used in situ observations of the ARTEMIS satellite to re-classify the dataset. All three datasets produced identical classifications due to the limited variability of the SW between L1 and the lunar orbit.

The actual classification was initially made through visual inspection and by comparing the statistical properties of each class to each event³⁶. However, to make our classification more robust and reproducible, we re-classified the dataset by using a supervised machine learning approach as discussed in ref. 38 and accessible through the code availability statement. Specifically, we used the same training set, which was carefully curated and analyzed in ref. 38 and we applied a machine learning Gaussian Process (GP) to classify probabilistically the dataset used. All the upstream datasets we used resulted in the same classification (i.e., the highest probability was consistently found to be in the same class). The code used to perform this operation can be found in the code availability statement.

In Table 2, we show the probabilities of each class for each event, while with bold text, one can find the highest probability which was used as the dominant class characterizing each event. Furthermore, in Supplementary Fig. 2 OMNIweb 1 h data are shown, describing the global picture of the solar wind conditions for the main seeded event and a non-seeded one (i.e., the #1 non-seeded of Fig. 3). The main event analyzed in the manuscript occurs a few hours after the beginning of a high-speed stream.

Diffusion time scales and spatial scale sizes

To estimate the diffusion time scales and compare them with the system scale sizes, we have used Bohm's diffusion formula⁶. This

formula is applicable when we have variations in the magnetic field that are in the same order as the background magnetic field values (i.e., $\delta B - B_0$). As shown in Figs. 1 and 2 and Supplementary Fig. 3, this is a systematic feature of the foreshock transients' core environment (i.e., the region between the trailing and leading compressive edge). Under this framework, the mean free path for pitch angle scattered electrons can be computed as $\lambda_{\max} \approx r_{ce}$ where r_{ce} is the electron gyroradius.

The diffusion length (L) can be estimated through the expression $L \approx D(E_{\max})/V_{sh}$, where $D(E_{\max})$ is the spatial diffusion coefficient for the maximum energy, and V_{sh} is the velocity of the shock in the spacecraft reference frame. Finally, the diffusion coefficient can be calculated $D(E_{\max}) = 1/3 \cdot v \cdot \lambda_{\max}$, where v is the velocity of the particles. Combining the above formulas, one can easily obtain an expression for the maximum diffusion length as:

$$L \approx 1/3 \cdot v/V_{sh} \cdot r_{ce} \quad (4)$$

In the above formula, we can use the relativistic kinetic energy expression, $E = (\gamma - 1)mc^2$, where m is the rest mass, c is the speed of light, and γ is the Lorentz factor. By expanding the Lorentz factor, and re-writing the kinetic energy expression, one can show that:

$$v = c \sqrt{1 - \left(\frac{mc^2}{E_{\max} + mc^2} \right)} \quad (5)$$

Using that expression, since we know the maximum energy, we can calculate the equivalent velocity and translate that to an effective electron gyroradius though $r_{ce} = \frac{mv}{eB_0}$ where e is the electric charge, and B_0 is the background magnetic field. Therefore, observationally, we can obtain a value for the electron gyroradius by measuring the energy of electrons and the background magnetic field. Finally, to compute the diffusion length, one needs to estimate the shock velocity. One can do that by timing the shock as it passes through the multiple MMS spacecraft. By performing the timing method^{20,21}, we obtain that the shock velocity in the spacecraft reference frame is in the order of $V_{sh} \sim 300$ km/s.

The background magnetic field at the core of a foreshock transient is in the order of 1 nT, as shown in Figs. 1, 2, and Supplementary Fig. 3, although in extreme cases it can reach values up to 10 nT. The maximum energy of electrons observed in our event is 523 keV for the main event analyzed in the manuscript. By using the above values, we obtain a diffusion length of $L = 10 - 100 R_e \approx 6 \cdot 10^{4-5}$ km, which is in agreement with the scale sizes of foreshock transients that have been observed in Earth's planetary environment (with $100 R_e$ corresponding to extreme cases)⁴⁵.

In order now to estimate what are the maximum obtainable energies in other planetary systems, we can take the typical scale sizes found in other planets along with typical background magnetic field observations⁴⁵. This energy corresponds to the maximum energy that an electron can have before its gyroradius gets so large that it cannot remain in the shock acceleration region and get further energized. We can assume that for giant planets like Jupiter, a foreshock transient scale size can reach values of $100 - 1000 R_e \approx 6 \cdot 10^{5-6}$ km. Using a background magnetic field value of 0.5–1 nT, it can be easily shown that the equivalent energy obtained from the electrons' gyroradius can be > 2 MeV.

Finally, to generalize our results to systems outside our solar system, some assumptions need to be made. Generally, the larger the system size (planet), the larger the maximum energy that can be sustained. Similarly, the stronger the magnetic field of the stellar wind, the higher the energy. As a result, one could investigate ultra-hot Jupiters as potential candidates in which electrons can achieve very high energies. These celestial objects are Jupiter-like exoplanets with very low orbital periods due to their proximity to their star⁴⁷.

If we assume a system size similar to Jupiter, we can obtain a foreshock transient scale size that can reach values of about $100 - 1000 R_e \approx 6 \cdot 10^{5-6}$ km. Now, depending on the age of the stellar system (young stellar systems have stronger magnetic fields embedded in their stellar wind), one can estimate the background magnetic field magnitude of the stellar wind near a planet close to the star to be in the order of $B \approx 0.01 - 1$ G = 10^{3-5} nT^{48,49}. By following the exact argument above, we can obtain that the maximum energy in these systems can be in the order of GeV to TeV. It should be noted that even when computing the synchrotron losses for these energy ranges and magnetic fields, the loss is insignificant. As observations and modeling efforts in these systems are highly susceptible to errors, one should treat the whole discussion here not as a direct comparison to other acceleration mechanisms but rather as a consequence of our model that needs further investigation by the astrophysics and exoplanet research communities.

Foreshock transient & shock characterization

While the characterization of the foreshock transients is out of the scope of this work, it should be noted that the majority of the transients shown in this work would have been classified as hot flow anomalies (HFAs) in heliophysics terminology. The exact characterization of these transients is out of the scope of this work and irrelevant to our findings as regardless of the exact nature, foreshock bubbles and HFAs have been found to be particularly efficient accelerators (see e.g.,^{14,17,25}). Furthermore, both types of phenomena contain all the necessary ingredients for our model (i.e., shock formation, compressive edges, high-frequency nonlinear waves, large amplitude waves associated with low-density regions to facilitate scattering, etc.)¹⁶.

To characterize the shock formed at the compressive edge of the foreshock transient (highlighted in Figs. 1 and 2), we used single-point and multipoint analysis techniques (see e.g., ref. 20 and code availability statements for openly accessible code to access these). All techniques, as expected from previous results, indicated that the fast shock formed at the sun-facing compressive edge of the foreshock structure is a typical quasi-perpendicular ($\theta_{Bn} > 45^\circ$) shock. Specifically, all the methods typically used in these studies (i.e., coplanarity theorem, timing, and minimum variance analysis)⁶² showed an angle systematically above 55 degrees similar to other similar foreshocks transient events²⁰.

Wavelet and wave-particle interaction analysis

For Fig. 2, we calculate the power spectral density (PSD) of the electric and magnetic fields using a wavelet transform, which allows us to observe how the power of the various oscillations is distributed in frequency and how it varies with time. Furthermore, to characterize the various wave modes excited we use singular value decomposition (SVD) to calculate the degree of polarization, ellipticity, and θ_{KB} , which are respectively a measure of the coherence of the waves, a measure of the handedness of the waves, and the angle between the wave vector (k) and the background magnetic field (B_0). The ellipticity has a value in the interval $[-1, 1]$ where values of -1, 0, and 1 reflect waves that are left-hand, linearly, or right-hand polarized respectively. The propagation angle (θ_{KB}) ranges between 0 and 90 degrees, with 0/90 representing parallel/perpendicular propagations with respect to B_0 .

The identification of the high-frequency whistler waves was mainly obtained by their typical frequency that lies within $[0.1, 1]f_{ce}$ with f_{ce} being the electron cyclotron frequency. To quantify the relative power of the wave activity, we integrated the PSD in frequency space for each interval of interest (compressive region of the foreshock transient). This approach allowed us to estimate the total magnetic field variability for the specific wave mode (δB^2). To evaluate how prominent the wave amplitude is compared to the background magnetic field and essentially quantify the nonlinearity of the wave, we

took the square root and divided it by the background field to obtain an estimate of, $\delta B/B_0$ which was used in Fig. 3. The exact values obtained from this methodology are shown in Table 2.

To evaluate the cyclotron resonance between the energetic electrons and the whistler waves, we need first to write the resonance condition: $\omega - k_z v_z + m\Omega_{ce} = 0^{42}$, where ω is the frequency of the wave, while k_z and v_z are the components of the wave vector and the electron velocity along the background magnetic field respectively, and Ω_{ce} is the electron gyrofrequency. In the main event presented, we estimate $\omega \sim 0.3 \Omega_{ce}$ which results in a frequency $f_{ce} \approx 500$ Hz calculated via $f = \frac{\omega}{2\pi}$. By using the cold plasma dispersion relations, the observed high-frequency whistlers have a wavelength of $\lambda = 25$ km. For the observed electrons of a realistic initial energy of 20 keV, the total velocity of the particles is estimated to be $v_e = 8.4 \cdot 10^7$ km/s. For such electrons to be in cyclotron resonance with the observed HF whistlers, the pitch angle (PA) of these electrons needs to be approximately 79°. Similarly, for a slightly higher energy of 50 keV, their PA needs to be around 83°. The interaction between the electrons is shown in Fig. 3, as the nonlinear resonance of the electrons will make them gain energy in the perpendicular direction which will further increase their PAs, reaching asymptotically 90°^{32,33}. As discussed in the Results section, during the strongest whistler activity, we see in the Pitch Angle distribution (Fig. 2h) an enhanced flux at PA 90° which is a signature of the above-mentioned resonant energization mechanism.

We should also note the acceleration process via wave-particle interaction discussed in this work is not related to quasi-linear theory and pitch angle diffusion (e.g., ref. 63). As written in the main manuscript, the resonance we highlight is between nonlinear waves and electrons (e.g., ref. 31). The nonlinear nature of these waves is evident from their relatively high amplitude compared to the background (see Fig. 3 and Table II) and their characteristic coherent narrowband emission^{34,64}. Having said that, acceleration mechanisms through resonance are found to be more efficient for low-density plasma with high magnetic fields (e.g., radiation belts). It has been shown that a way to quantify the efficiency of the acceleration obtained through this mechanism is by looking at the ratio between the electron plasma frequency (f_{pe}) and the gyrofrequency (f_{ce}). The ratio in the radiation belt can be close to unity (see, e.g., ref. 63) while in typical foreshock plasma, it can be on the order of magnitudes higher. However, due to the special plasma conditions of foreshock transients, the core (Fig. 1, blue-shaded region) contains very low-density plasma, while the shock (Fig. 1, green-shaded area) contains a magnetic field that, due to compression is higher than the typical foreshock. These combined allow this ratio for our main event to be in the order of $f_{pe}/f_{ce} \sim 30$ when considering the bulk properties. Considering partial distributions, which are more accurate in shock/foreshock environments, should decrease the density and, therefore, also the f_{pe}/f_{ce} ratio (see e.g., ref. 65) even more. Furthermore, although the efficiency of wave-particle interactions may not be as pronounced as in very low-density plasma environments, recent studies have demonstrated that these interactions can still contribute to the energization and scattering of electrons in a foreshock transient^{30,66}. Moreover, when moving to exoplanetary systems with stronger magnetic fields (e.g., ultra-hot Jupiters⁴⁷) this ratio is decreased, which further supports the generalization of our model to other environments. Finally, while it remains uncertain whether interactions between electrons and high-frequency whistlers will average out to a quasi-linear picture, the nonlinear characteristics observed in the waves suggest deviations from classical resonance theory, given that for all events we observe a $\delta B/B_0 \approx 1 - 10\%$.

Occurrence and probability analysis of foreshock transients

As briefly mentioned in the main text, foreshock transient phenomena can be present in every planetary environment within a stellar system and occur very frequently¹⁵. However, obtaining actual in situ

observations in our solar system of all the elements of the presented mechanism is heavily influenced by various statistical and orbital effects, qualitatively discussed below.

The first statistical issue affecting our observational capabilities is the probability of observing fast solar wind (coronal hole) plasma corresponding to the conditions we verified as necessary to have a prominent electron seed population (1–5 keV range), highlighted throughout the main text. Coronal hole plasma consists of roughly 20% of the total solar wind measurements based on Lagrangian 1 (L1) point observations (refs. 36–38). In addition, fast solar wind is associated with more frequent magnetic field discontinuities³⁹, and the occurrence rate of such a discontinuity is roughly in the order of 1–10 every hour⁴⁰. These effects show that while foreshock transients can form with an occurrence of hours¹⁵, seeded events exhibiting significant electron acceleration like the one we describe may have an occurrence rate in the order of days.

Having said that, from an observational point of view, to measure the seeded population (ARTEMIS) and the foreshock transient (MMS), both spacecraft need to be at a specific location in their orbit.

MMS spacecraft is in the ion foreshock for around 10% of its lifetime, although this heavily varies based on its orbit. Furthermore, in order to do the analysis required in this manuscript, MMS has to acquire high-time resolution measurements (i.e., burst data) that are typically unavailable during foreshock observations, making this percentage lower. Moreover, to observe these phenomena, it is not just sufficient to be in the foreshock at the right time, but also to observe the foreshock transient after it has been fully formed, which reduces the occurrence even more. Moving on to the ARTEMIS mission in lunar orbit, it can provide far upstream measurements for less than 50% of the time, as for the rest of the time it is on the nightside of the Earth or very close to the shock. This results in a net probability of observing such a foreshock transient to be less than 1–5% even considering the most conservative estimations. As a result, while these phenomena can occur very frequently¹⁵, the observational capabilities we currently have, allow us to observe only a few conjunction events per year.

All the effects listed above are the reason that a detailed investigation of several years of data resulted in 6 seeded cases that were analyzed in Fig. 3. Our research targets the detection of high-energy electrons, enabling us to identify specific acceleration events. However, it is crucial to recognize that non-energetic events can still occur under the influence of coronal hole (CH) solar wind. Factors such as suboptimal geometry, limited wave-particle interactions, and insufficient compression can constrain substantial electron acceleration. As a result, significant electron acceleration might not always be observed, even in the presence of CH solar wind.

Statistical analysis details

In this work, we focused on analyzing the most energetic event (i.e., the one shown in Figs. 1 and 2 and #1 seeded in Fig. 3) which highlights all the components of the presented acceleration model. However, for the statistical verification of our work, we examined multiple cases that contained partially or fully the components of our model (Fig. 3). In Supplementary Fig. 3, we show an overview plot of an event that was compared with the main event (i.e., #1 non-seeded on Fig. 3). There, one can see that a well-formed foreshock transient that lacks the initial seeded population from the solar wind results in no observable electron acceleration (Supplementary Fig. 3d). This is also the event that was compared side by side with the main event in Fig. 4.

Furthermore, for verification and to make our work reproducible, a table with all the dates for each event as measured by MMS along with the associated ARTEMIS upstream observations are provided (Table 3). The intervals shown there were used to obtain the maximum flux ratio compared to the surroundings that were used in Figs. 3 and 4.

It should be noted that for the determination of the magnetic field discontinuity responsible for the formation of each foreshock

Table 3 | Time intervals and positions (in GSE coordinates) for all presented events corresponding to MMS and ARTEMIS measurements

MMS (GSE)	MMS (Start UTC)	MMS (Stop UTC)	ARTEMIS (GSE)	ARTEMIS (Start UTC)	ARTEMIS (Stop UTC)	
#1 seed	10.8, 11.1, 5.1	2017-12-17 17:52:00	2017-12-17 17:54:00	65.2, -5.3, 5.1	2017-12-17 17:39:00	2017-12-17 17:43:00
#2 seed	10.2, -6.0, 5.9	2021-02-13 11:05:00	2021-02-13 11:06:10	57.6, 18.6, -4.9	2021-02-13 11:02:00	2021-02-13 11:10:00
#3 seed	8.7, 17.0, 4.7	2018-12-10 06:27:00	2018-12-10 06:31:00	50.1, 35.6, -0.2	2018-12-10 06:16:00	2018-12-10 06:19:00
#4 seed	16.6, 1.9, 6.3	2019-01-05 17:38:00	2019-01-05 17:41:00	63.3, -3.5, 1.3	2019-01-05 17:20:00	2019-01-05 17:35:00
#5 seed	9.3, 17.4, 4.9	2018-12-10 05:12:00	2018-12-10 05:25:00	50.4, 35.3, -0.1	2018-12-10 05:17:00	2018-12-10 05:23:00
#6 seed	9.6, 17.6, 5.0	2018-12-10 04:40:00	2018-12-10 04:42:00	50.7, 35.0, -0.1	2018-12-10 04:20:00	2018-12-10 04:37:00
#1 no-seed	15.2, 5.6, 5.2	2018-01-12 01:50:00	2018-01-12 01:52:30	38.0, -49.4, 5.1	2018-01-12 01:35:00	2018-01-12 01:45:00
#2 no-seed	8.7, 12.2, -8.1	2023-01-16 08:21:00	2023-01-16 08:24:00	13.1, -55.9, -0.3	2023-01-16 08:05:00	2023-01-16 08:15:00
#3 no-seed	11.7, 12.2, -5.6	2021-01-12 01:18:00	2021-01-12 01:21:00	58.2, -17.3, -1.1	2021-01-12 00:56:00	2021-01-12 01:01:00
#4 no-seed	1.6, -24.8, -1.5	2022-05-02 18:23:00	2022-05-02 18:25:00	61.2, 22.2, 1.3	2022-05-02 17:55:00	2022-05-02 18:03:00
#5 no-seed	-2.3, 23.4, -9.5	2022-11-24 04:16:00	2022-11-24 04:18:00	55.1, 22.2, 1.3	2022-11-24 03:48:00	2022-11-24 03:54:00
#6 no-seed	14.4, 7.4, 6.1	2018-12-14 04:21:00	2018-12-14 04:22:00	16.1, 61.9, -3.8	2018-12-14 04:00:00	2018-12-14 04:10:00

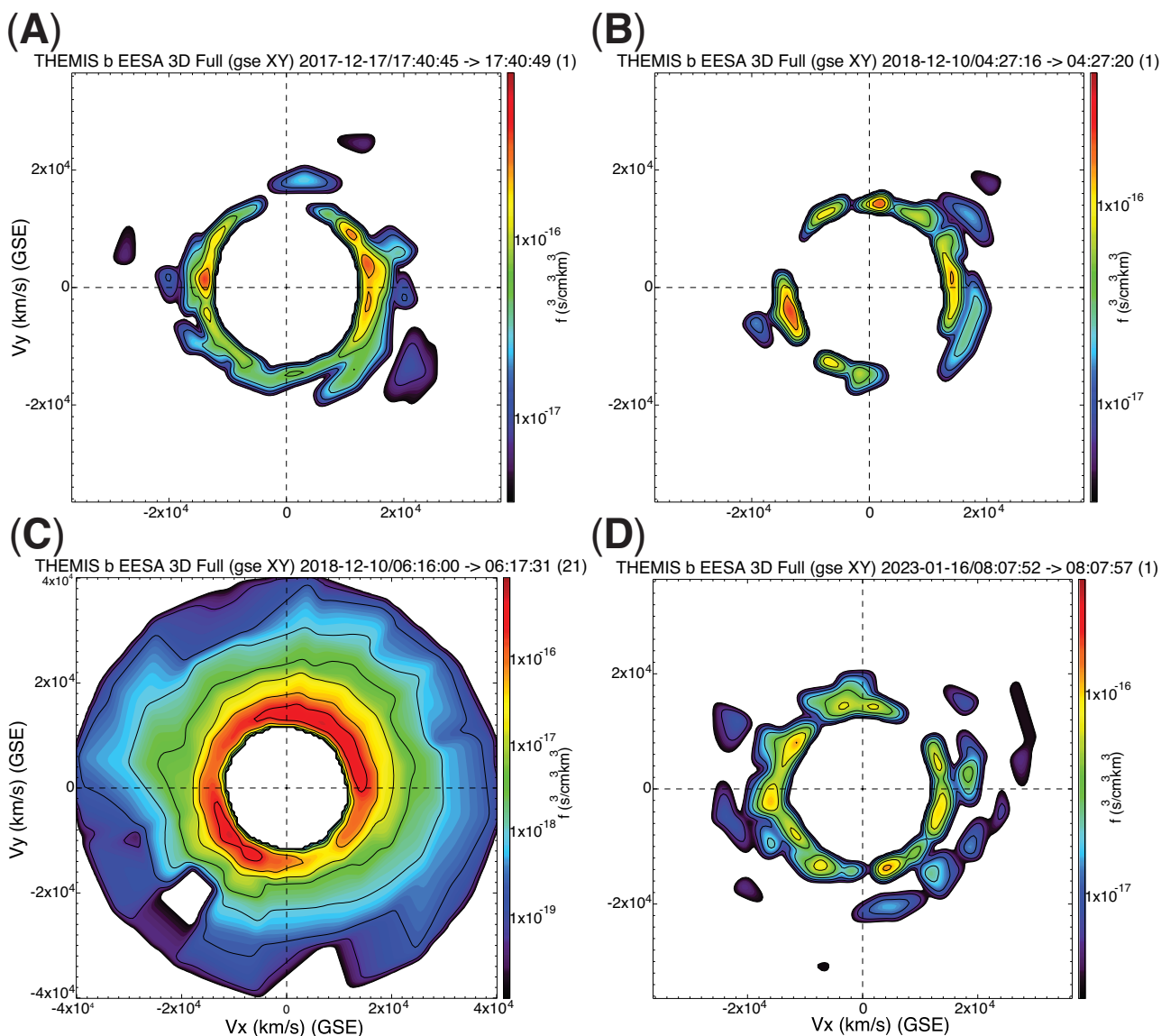


Fig. 5 | 2D distribution slices for selected ARTEMIS events. 2D distribution slices in velocity space in GSE coordinates, showing ARTEMIS observations for three seeded and one non-seeded event (namely, (A) for #1, (B) for #6, (C) for #3, and (D) for #2 no-seed). The X-axis shows the velocity along X GSE coordinates (Earth-Sun

line). These ring-like distributions indicate that the electron population is traveling towards and from the Earth. The slices are obtained by restricting the energy between 500 and 5000 eV in order to be directly associated with the seed population discussed in the manuscript.

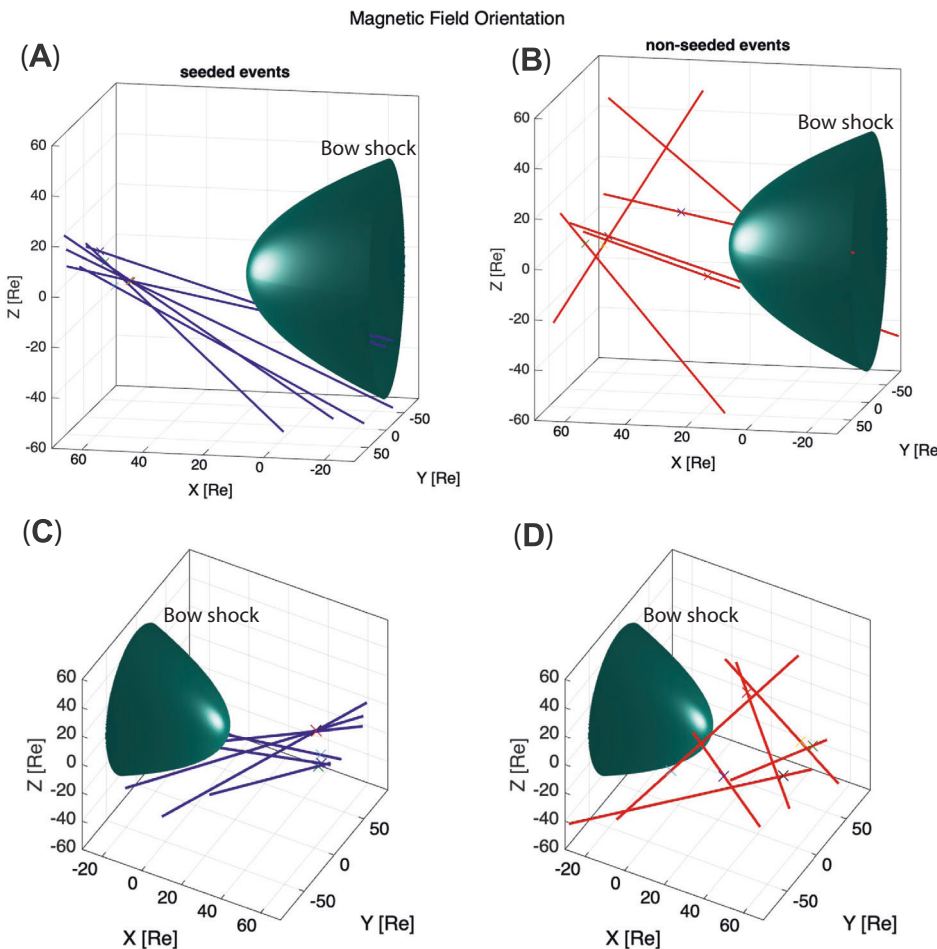


Fig. 6 | Bow shock modeling and magnetic connectivity. 3D bow shock model using⁶⁹ under typical solar wind conditions. **A** shows the location of ARTEMIS and the magnetic field lines in GSE coordinates during the maximum electron flux for the suprathermal-seed energy range (see Table 3). As shown here, only 2 out of the

6 seeded events appear to be connected to the bow shock. **B** the same plot but for the non-seeded event. **C** and **D** follow the same format but from a different point of view. In this case, one out of 6 magnetic field lines is connected to the Earth's bow shock.

transient, we used a multi-step process. First, based on the position of the two spacecraft, we estimated an approximate time lag by using the solar wind velocity as measured by MMS. Then we determined whether a magnetic field rotation was observed before and after the foreshock transient at MMS. Using the rotation associated with the foreshock transient, we proceed to cross-validate our findings with the magnetic field rotations occurring within the time-lagged interval at the ARTEMIS dataset. This resulted in an associated discontinuity at ARTEMIS orbit occurring from 2 to up to 20 minutes before the MMS observations. After confirming the magnetic disturbance per event, we limited the time interval to within - 5 minutes of the observations and obtained the background value by evaluating steady solar wind calm conditions within a 20-minute window. As shown in Table 3, the relative position of MMS with respect to ARTEMIS can have a wide range of values. This, along with the fact that the orientation of the normal of the discontinuity can be at the same plane as the separation vector between MMS and ARTEMIS, allows the time lag in certain cases to be relatively small, or even instantaneous (e.g., event #5). Since the discontinuity can interact with Earth's bow shock and form a foreshock transient at the same time as observed by ARTEMIS, these cases are statistically expected.

At this point, we should stress that for the events occurring on 2018-12-10 (i.e., #3, #5, #6) the high-energy electron instrument of ARTEMIS (SST) observed 100s keV electrons. For the rest of the events, either the data quality of the instrument showed faulty data and/or no

high-energy electrons were measured. This suggests that the electrons accelerated from the presented mechanism, as expected, can be scattered and travel both sunward and earthward.

Finally, as mentioned in the main text, apart from the solar origin, the seed population can be associated with the presence of an extended electron foreshock. An exclusive foreshock origin seems unlikely since the electron foreshock is always present, and this could not explain why, in well-developed transients (see Supplementary Fig. 3), with clear shock formation and wave activity there is no noticeable particle acceleration. However, electron foreshock can likely contribute to the seed population as reflected particles from the planetary bow shock can get scattered and interact with the upstream foreshock transient (see e.g., relevant articles on ions^{13,25}).

To evaluate this possibility, we first investigated the partial distribution function for the low keV seed population observed at ARTEMIS orbit (Fig. 5). For all events, we see particles between the seed energy range (~ 1–5 keV) to form a ring-like distribution in the XY GSE plane. This type of distribution could be considered a part of a Bi-Maxwellian like distribution that hints towards a clear solar origin. However, it could be part of the electron distribution originating from particles reflected from the nearby Earth's bow shock (i.e., electron foreshock). This, while still a possibility, is not very likely. By examining the distribution one can see that the events exhibiting these features are associated with low statistics, both because the instrument mode has a low sampling frequency, but also because of the limitation on

energy range¹⁹. This is illustrated in Fig. 5C, where an event with another instrument mode activated allows more frequent measurements, indicating the presence of a typical thermalized SW type distribution being present. Another test is to compare the distribution found in seeded events with the non-seeded ones (e.g., Fig. 5D). As shown there, the distributions of the seeded events (panels A, B) are very similar to the ones with the non-seeded ones except for enhanced PSD indicating both earthward and sunward particles. This hints towards a complex interplay in which both solar and foreshock origin particles may be present. It is important to note that beam-like distributions are evident in the seeded events, as depicted in Fig. 5A, B. This observation indicates that, in addition to potential contributions from the foreshock, instabilities within the solar wind may also contribute to the formation of the seed population^{67,68}.

Moving on, we evaluate if a link between solar wind observations and connectivity to Earth's bow shock exists. This is done to determine whether a systematic connection to the electron foreshock exists across all seeded events. If such a consistent connection is found, it would imply that the reflected foreshock population may be the primary mechanism driving the observed seed population. Through a 3D bow shock model⁶⁹, we used the magnetic field orientation for both seeded and non-seeded events and investigated whether they intersected the bow shock surface. As shown in Fig. 6, 2 out of 6 seeded events and 1 out of 6 non-seeded events appear to be unambiguously mapped to the bow shock. For the seeded events, we took the magnetic field orientation during the peak of the suprathermal electron flux. For the non-seeded events, since there is no significant enhancement in electron flux, we took the magnetic field orientation before the discontinuity (taking the magnetic field data after the discontinuity produced the same results). The analysis shown in Fig. 6 shows that the electron foreshock cannot be the only source of suprathermal electrons. It does show, however, that seeded events that experience significant acceleration of electrons have discontinuities for which the geometry is optimal for the formation of foreshock transients. The orientation of these field lines (Fig. 6A) essentially allows the intersection point with the shock to slowly move across the bow shock as the field lines get convected with the nominal solar wind. This illustrates the geometrical effect that the foreshock transients can have on further enhancing the acceleration process discussed in the main text and illustrated in Fig. 4.

Data availability

The MMS data are archived at <https://lasp.colorado.edu/mms/sdc/public/>. The THEMIS/ARTEMIS data can be found at https://themis.ssl.berkeley.edu/data_products/index.php, while the OMNIweb data is accessed through <https://spdf.gsfc.nasa.gov/pub/data/omni/>. Information about the level, calibration, and instrumentation used for each quantity can be found in the method, subsection data. All calculations shown and reported in this work are done with the open-access data available from each mission as a level-2 calibrated dataset. The post-processed data supporting the findings of this study, specifically the non-time series data (i.e., Figs. 2i and 3), are provided as source data to facilitate easier reproducibility. The remaining post-processed data are available from the corresponding author upon request. Source data are provided in this paper.

Code availability

The analysis of the work was done via the PySPEDAS (<https://github.com/spedas/pyspedas/tree/master>)⁷⁰, SPEDAS (<http://spedas.org/blog/>)⁷¹ and IRFU-Matlab (<https://github.com/irfu/irfu-matlab/tree/master>)⁷² libraries. Specifically, PySPEDAS was used to download the observations and IRFU-Matlab to analyze and process the files for the plots and the analysis shown in the manuscript. One can access the version of the codes used along with instructions on how to reproduce each figure and table of our work on the associated Zenodo repository <https://zenodo.org/records/14048045>⁷³ or directly from the GitHub repository <https://github.com/SavvasRaptis/Relativistic-Electrons-Foreshock>. Alternatively, all the software listed above is openly available through their official repository. In addition, we made use of the machine learning code openly available on ref. 38 and on the hosting website of the corresponding author <https://ecamporeale.github.io/codes.html> by following https://ecamporeale.github.io/software/OMNI2_classification.dat provides the training dataset for the code, https://ecamporeale.github.io/software/classify_solar_wind.m shows a working code example, and https://ecamporeale.github.io/software/parameters_classification.mat contains the parameters required to run the model. Finally, we used a 3D bow shock model, openly described in ref. 69. Its implementation in MATLAB is straightforward and can be made available from the corresponding author upon request.

References

- Chen, B. et al. Particle acceleration by a solar flare termination shock. *Science* **350**, 1238 (2015).
- O'C. Drury, L. An introduction to the theory of diffusive shock acceleration of energetic particles in tenuous plasmas. *Rep. Prog. Phys.* **46**, 973 (1983).
- Blasi, P. The origin of galactic cosmic rays. *Astron. Astrophys. Rev.* **21**, 70 (2013).
- Masters, A. et al. Electron acceleration to relativistic energies at a strong quasi-parallel shock wave. *Nat. Phys.* **9**, 164 (2013).
- Fiuza, F. et al. Electron acceleration in laboratory-produced turbulent collisionless shocks. *Nat. Phys.* **16**, 916 (2020).
- Caprioli, D. & Spitkovsky, A. Simulations of ion acceleration at non-relativistic shocks. iii. particle diffusion. *Astrophys. J.* **794**, 47 (2014).
- Ball, L. & Melrose, D. Shock drift acceleration of electrons. *Publ. Astron. Soc. Aust.* **18**, 361 (2001).
- Blandford, R. D. & Ostriker, J. P. Particle acceleration by astrophysical shocks. *Astrophys. J.* **221**, L29 (1978).
- Park, J., Caprioli, D. & Spitkovsky, A. Simultaneous acceleration of protons and electrons at nonrelativistic quasiparallel collisionless shocks. *Phys. Rev. Lett.* **114**, 085003 (2015).
- Matsumoto, Y., Amano, T., Kato, T. & Hoshino, M. Stochastic electron acceleration during spontaneous turbulent reconnection in a strong shock wave. *Science* **347**, 974 (2015).
- Shalaby, M., Lemmerz, R., Thomas, T. & Pfrommer, C. The mechanism of efficient electron acceleration at parallel non-relativistic shocks. *Astrophys. J.* **932**, 86 (2022).
- Caprioli, D. & Spitkovsky, A. Simulations of ion acceleration at non-relativistic shocks. i. acceleration efficiency. *Astrophys. J.* **783**, 91 (2014).
- Turner, D. et al. Autogenous and efficient acceleration of energetic ions upstream of earth's bow shock. *Nature* **561**, 206 (2018).
- Liu, T. Z., Angelopoulos, V. & Lu, S. Relativistic electrons generated at earth's quasi-parallel bow shock. *Sci. Adv.* **5**, eaaw1368 (2019).
- Schwartz, S. J. et al. Conditions for the formation of hot flow anomalies at earth's bow shock. *J. Geophys. Res. Space Phys.* **105**, 12639 (2000).
- Zhang, H. et al. Dayside transient phenomena and their impact on the magnetosphere and ionosphere. *Space Sci. Rev.* **218**, 40 (2022).
- Wilson III, L. B. et al. Relativistic electrons produced by foreshock disturbances observed upstream of earth's bow shock. *Phys. Rev. Lett.* **117**, 215101 (2016).
- Burch, J., Moore, T., Torbert, R. & Giles, B.-h Magnetospheric multiscale overview and science objectives. *Space Sci. Rev.* **199**, 5 (2016).
- Angelopoulos, V. *The ARTEMIS Mission* (2014).
- Turner, D. L. et al. Direct multipoint observations capturing the reformation of a supercritical fast magnetosonic shock. *Astrophys. J. Lett.* **911**, L31 (2021).

21. Amano, T. et al. Observational evidence for stochastic shock drift acceleration of electrons at the earth's bow shock. *Phys. Rev. Lett.* **124**, 065101 (2020).
22. Axford, W., Leer, E., & Skadron, G. in *International Cosmic Ray Conference* **11**, 132–137 (Springer, 1977).
23. Longair, M. S. *High Energy Astrophysics* (Cambridge University Press, 2011).
24. Oka, M. et al. Electron power-law spectra in solar and space plasmas. *Space Sci. Rev.* **214**, 82 (2018).
25. Liu, T. Z., Lu, S., Angelopoulos, V., Hietala, H. & Wilson III, L. B. Fermi acceleration of electrons inside foreshock transient cores. *J. Geophys. Res. Space Phys.* **122**, 9248 (2017).
26. Shi, X., Liu, T. Z., Angelopoulos, V. & Zhang, X.-J. Whistler mode waves in the compressional boundary of foreshock transients. *J. Geophys. Res. Space Phys.* **125**, e2019JA027758 (2020).
27. Vasko, I. et al. Solitary waves across supercritical quasi-perpendicular shocks. *Geophys. Res. Letters* **45**, 5809 (2018).
28. Kamaletdinov, S., Yushkov, E., Artemyev, A., Lukin, A., & Vasko, I. Superthin current sheets supported by anisotropic electros. *Phys. Plasmas* **27**, 082904 (2020).
29. Kamaletdinov, S. R., Vasko, I. Y. & Artemyev, A. V. Nonlinear electron scattering by electrostatic waves in collisionless shocks. *J. Plasma Phys.* **90**, 905900201 (2024).
30. Shi, X., Liu, T., Artemyev, A., Angelopoulos, V., Zhang, X.-J. & Turner, D. L. Intense whistler-mode waves at foreshock transients: Characteristics and regimes of wave-particle resonant interaction. *Astrophys. J.* **944**, 193 (2023).
31. Bortnik, J., Thorne, R. & Inan, U. S. Nonlinear interaction of energetic electrons with large amplitude chorus. *Geophys. Res. Lett.* **35**, <https://doi.org/10.1029/2008GL035500> (2008).
32. Thorne, R. E. et al. Rapid local acceleration of relativistic radiation-belt electrons by magnetospheric chorus. *Nature* **504**, 411 (2013).
33. Horne, R. B. Resonant diffusion of radiation belt electrons by whistler-mode chorus. *Geophys. Res. Lett.* **30**, <https://doi.org/10.1029/2003GL016963> (2003).
34. Artemyev, A. et al. Electron resonant interaction with whistler waves around foreshock transients and the bow shock behind the terminator. *J. Geophys. Res. Space Phys.* **127**, e2021JA029820 (2022).
35. Feldman, U., Landi, E., and Schwadron, N. On the sources of fast and slow solar wind. *J. Geophys. Res. Space Phys.* **110**, <https://doi.org/10.1029/2004JA010918> (2005).
36. Xu, F. & Borovsky, J. E. A new four-plasma categorization scheme for the solar wind. *J. Geophys. Res. Space Phys.* **120**, 70 (2015).
37. Borovsky, J. E. The plasma structure of coronal hole solar wind: Origins and evolution. *J. Geophys. Res. Space Phys.* **121**, 5055 (2016).
38. Camporeale, E., Carè, A. & Borovsky, J. E. Classification of solar wind with machine learning. *J. Geophys. Res. Space Phys.* **122**, 10 (2017).
39. Tsurutani, B. T. & Ho, C. M. A review of discontinuities and Alfvén waves in interplanetary space: Ulysses results. *Rev. Geophys.* **37**, 517 (1999).
40. Liu, Y. et al. Magnetic discontinuities in the solar wind and magnetosheath: Magnetospheric multiscale mission (mms) observations. *Astrophys. J.* **930**, 63 (2022).
41. Gosling, J., Skoug, R., McComas, D., & Smith, C. Direct evidence for magnetic reconnection in the solar wind near 1 au. *J. Geophys. Res. Space Phys.* **110**, <https://doi.org/10.1029/2004JA010809> (2005).
42. Breech, B., Matthaeus, W. H., Cranmer, S., Kasper, J., & Oughton, S. Electron and proton heating by solar wind turbulence. *J. Geophys. Res. Space Phys.* **114**, <https://doi.org/10.1029/2009JA014354> (2009).
43. Shen, Y., Artemyev, A., Angelopoulos, V., Liu, T. Z. & Vasko, I. Comparing plasma anisotropy associated with solar wind discontinuities and Alfvénic fluctuations. *Astrophys. J.* **961**, 41 (2024).
44. Raouafi, N. E. et al. Magnetic reconnection as the driver of the solar wind. *Astrophys. J.* **945**, 28 (2023).
45. Valek, P. et al. Hot flow anomaly observed at Jupiter's bow shock. *Geophys. Res. Lett.* **44**, 8107 (2017).
46. Masters, A. et al. Hot flow anomalies at Saturn's bow shock. *J. Geophys. Res. Space Phys.* **114**, <https://doi.org/10.1029/2009JA014112> (2009).
47. Cauley, P. W., Shkolnik, E. L., Llama, J. & Lanza, A. F. Magnetic field strengths of hot Jupiters from signals of star-planet interactions. *Nat. Astron.* **3**, 1128 (2019).
48. Nichols, J. & Milan, S. Stellar wind-magnetosphere interaction at exoplanets: computations of auroral radio powers. *Mon. Not. R. Astron. Soc.* **461**, 2353 (2016).
49. Chebly, J. J., Alvarado-Gómez, J. D., Poppenhäger, K. & Garraffo, C. Numerical quantification of the wind properties of cool main sequence stars. *Mon. Not. R. Astron. Soc.* **524**, 5060 (2023).
50. Turner, D., Omidi, N., Sibeck, D. & Angelopoulos, V. First observations of foreshock bubbles upstream of Earth's bow shock: Characteristics and comparisons to HFS. *J. Geophys. Res. Space Phys.* **118**, 1552 (2013).
51. Li, J.-H. et al. Identification of coupled Landau and anomalous resonances in space plasmas. *Phys. Rev. Lett.* **133**, 035201 (2024).
52. Oka, M. et al. Electron scattering by high-frequency whistler waves at Earth's bow shock. *Astrophys. J. Lett.* **842**, L11 (2017).
53. Collinson, G. et al. A survey of hot flow anomalies at Venus. *J. Geophys. Res. Space Phys.* **119**, 978 (2014).
54. Collinson, G. et al. A hot flow anomaly at Mars. *Geophys. Res. Lett.* **42**, 9121 (2015).
55. Reynolds, S. P. Particle acceleration in supernova-remnant shocks. *Astrophys. Space Sci.* **336**, 257 (2011).
56. Hospodarsky, G. B. et al. Jovian bow shock and magnetopause encounters by the Juno spacecraft. *Geophys. Res. Lett.* **44**, 4506 (2017).
57. Ray, T. P. et al. Outflows from the youngest stars are mostly molecular. *Nature* **622**, 48 (2023).
58. Chang, J. et al. An excess of cosmic ray electrons at energies of 300–800 GeV. *Nature* **456**, 362 (2008).
59. Archer, A. et al. Measurement of cosmic-ray electrons at TeV energies by VERITAS. *Phys. Rev. D* **98**, 062004 (2018).
60. Crumley, P., Caprioli, D., Markoff, S. & Spitkovsky, A. Kinetic simulations of mildly relativistic shocks—I. particle acceleration in high Mach number shocks. *Mon. Not. R. Astron. Soc.* **485**, 5105 (2019).
61. Hilmer, R., Ginet, G. & Cayton, T. Enhancement of equatorial energetic electron fluxes near $L=4.2$ as a result of high speed solar wind streams. *J. Geophys. Res. Space Phys.* **105**, 23311 (2000).
62. Paschmann, G. & Schwartz, S. ISSI book on analysis methods for multi-spacecraft data, in *Cluster-II Workshop Multiscale/Multipoint Plasma Measurements* Vol. 449 (2000).
63. Allison, H. J., Shprits, Y. Y., Zhelavskaya, I. S., Wang, D. & Smirnov, A. G. Gyroresonant wave-particle interactions with chorus waves during extreme depletions of plasma density in the van Allen radiation belts. *Sci. Adv.* **7**, eabc0380 (2021).
64. Zhang, Y., Matsumoto, H. & Kojima, H. Whistler mode waves in the magnetotail. *J. Geophys. Res. Space Phys.* **104**, 28633 (1999).
65. Raptis, S. et al. Downstream high-speed plasma jet generation as a direct consequence of shock reformation. *Nat. Commun.* **13**, 598 (2022).
66. Vargas, A. D., Artemyev, A. V., Zhang, X.-J., & Albert, J. Role of “positive phase bunching” effect for long-term electron flux dynamics due to resonances with whistler-mode waves. *Phys. Plasmas* **30**, 112905 (2023).
67. Lin, R. Wind observations of suprathermal electrons in the interplanetary medium. *Space Sci. Rev.* **86**, 61 (1998).
68. Verscharen, D. et al. Electron-driven instabilities in the solar wind. *Front. Astron. Space Sci.* **9**, 951628 (2022).
69. Chapman, J. & Cairns, I. H. Three-dimensional modeling of Earth's bow shock: Shock shape as a function of Alfvén Mach number. *J.*

- Geophys. Res. Space Phys. **108**, <https://doi.org/10.1029/2002JA009569> (2003).
70. Grimes, E. W. et al. The space physics environment data analysis system in python. *Front. Astron. Space Sci.* **9**, 1020815 (2022).
71. Angelopoulos, V. et al. The space physics environment data analysis system (spedas). *Space Sci. Rev.* **215**, 1 (2019).
72. Khotyaintsev, Y. et al. irfu/irfu-matlab: v1.16.3, <https://doi.org/10.5281/zenodo.11550091> (2024).
73. Raptis, S. SavvasRaptis/Relativistic-Electrons-Foreshock: Relativistic-Electrons-Foreshock: Initial release. <https://doi.org/10.5281/zenodo.14048045> (2024).

Acknowledgements

This work was supported by the Magnetospheric Multiscale (MMS) mission of NASA's Science Directorate Heliophysics Division via a subcontract to the Southwest Research Institute (NNG04EB99C). SR acknowledges additional funding from NASA DRIVE Science Center for Geospace Storms (CGS) - 80NSSC22M0163, and Johns Hopkins University Applied Physics Laboratory independent R&D fund. SR acknowledges the support of the International Space Sciences Institute (ISSI) team 555: Impact of Upstream Mesoscale Transients on the Near-Earth Environment, and the Archival Research Visitor Program of the European Space Agency (ESA). AL acknowledges funding from the Swedish Research Council grant 2018-05514. M.L. acknowledges the support of the International Space Science Institute (ISSI) in Bern, through ISSI International Team Project 520 and funding from the Swedish Research Council grant 2018-05514 and the Royal Society awards RF\ERE\210353 and RF\ERE\231151. D.L.T. is thankful for funding from NASA's MMS and IMAP missions. D.L.T. also acknowledges funding from the National Science Foundation (NSF) Geospace Environment Modeling (GEM) program 2225463. DC acknowledges funding from NASA H-TMS grant 80NSSC20K1273, NASA H-TMS grant 80NSSC24K0173, and NSF-DoE grant PHY-2010240. We acknowledge the useful discussions with Anton Artemyev and Florian Koller. We also acknowledge Vassilis Angelopoulos, the instrument PIs and the whole team for use of data from the THEMIS/ARTEMIS mission. Finally, we acknowledge the entire Magnetospheric Multiscale team and instrument PIs for data access and support.

Author contributions

S.R., A.L., M.L., and D.L.T. conceptualized the study and initialized the work. S.R., A.L., M.L., D.L.T., and D.C. contributed to the methodology of the work. The analysis was done by S.R., A.L., M.L., D.L.T., and D.C.

Figures were generated by S.R., while visualization input was provided by S.R., A.L., M.L., D.L.T., and J.L.B. Funding acquisition was made by all the authors of the work. The original draft was written by S.R. with input from all the authors.

Competing interests

The authors declare no competing interests.

Additional information

Supplementary information The online version contains supplementary material available at <https://doi.org/10.1038/s41467-024-55641-9>.

Correspondence and requests for materials should be addressed to Savvas Raptis.

Peer review information *Nature Communications* thanks the anonymous reviewers for their contribution to the peer review of this work. A peer review file is available.

Reprints and permissions information is available at <http://www.nature.com/reprints>

Publisher's note Springer Nature remains neutral with regard to jurisdictional claims in published maps and institutional affiliations.

Open Access This article is licensed under a Creative Commons Attribution-NonCommercial-NoDerivatives 4.0 International License, which permits any non-commercial use, sharing, distribution and reproduction in any medium or format, as long as you give appropriate credit to the original author(s) and the source, provide a link to the Creative Commons licence, and indicate if you modified the licensed material. You do not have permission under this licence to share adapted material derived from this article or parts of it. The images or other third party material in this article are included in the article's Creative Commons licence, unless indicated otherwise in a credit line to the material. If material is not included in the article's Creative Commons licence and your intended use is not permitted by statutory regulation or exceeds the permitted use, you will need to obtain permission directly from the copyright holder. To view a copy of this licence, visit <http://creativecommons.org/licenses/by-nc-nd/4.0/>.

© The Author(s) 2025